Navier-Stokes Calculations of Hovering Rotor Flowfields

G. R. Srinivasan*
JAI Associates, Inc., Mountain View, California
and
W. J. McCroskey†
NASA Ames Research Center, Moffett Field, California

Unsteady, thin-layer Navier-Stokes equations written in rotor coordinates are solved using a partially flux-split, implicit numerical algorithm to calculate the flowfields of a hovering rotor blade at subsonic and transonic conditions. Numerical results are in good agreement with experimental data for both nonlifting and lifting rectangular blades. For the lifting case, the rotor wake effects are modeled by applying a correction to the geometric angle of attack of the blades. Alternate methods of calculating the hovering rotor flowfields in blade-fixed mode that have the same circulation distribution as a hovering blade are explored. All of the results presented in this paper were computed on a Cray-2 supercomputer.

Nomenclature

a_∞ = characteristic velocity scale, speed of sound
C = characteristic length scale, chord of the blade
C_L = lift coefficient
C_p = pressure coefficient
C_T = thrust coefficient
e = total energy per unit volume
$\hat{F},\hat{G},\hat{H}$ = flux vectors
$M(y)$ = Mach number along the blade span
M_∞ = freestream Mach number
M_{tip} = tip Mach number of the rotor blade
p = static pressure
Pr = Prandtl number
$\hat{Q}$ = flowfield vector
R = rotor radius
$R(t)$ = rotational matrix, see Eq. (7)
Re = Reynolds number
$\hat{S}$ = viscous flux vector
u_∞ = freestream velocity
u_{tip} = tip speed of the rotor blade
u,v,w = velocity components
U,V,W = contravariant velocity components
x,y,z,t = inertial coordinates
$\tilde{x},\tilde{y},\tilde{z},\tilde{t}$ = blade attached coordinates
α = angle of attack, degrees
γ = ratio of specific heats
Γ_V = dimensionless strength of tip vortex, normalized by u_∞ or u_{tip} and C
θ = pitch angle of the blade
$\theta(y)$ = pitch along the blade span
θ_{eff} = effective blade pitch angle
μ = viscosity coefficient
ξ,η,ζ,τ = generalized curvilinear coordinates
Ω = angular velocity of the rotor

Presented as Paper 87-2629-CP at the AIAA Atmospheric Flight Mechanics Conference, Monterey, CA, Aug. 17-19, 1987; received Sept. 30, 1987; revision received Feb. 13, 1988.

*Senior Research Scientist. Associate Fellow AIAA.
†Senior Staff Scientist, U.S. Army, Aeroflightdynamics Directorate. Associate Fellow AIAA.

Introduction

THE need to accurately calculate the flowfield of a helicopter rotor in both hover and forward flight is of great practical importance. Unlike the flowfield of a fixed wing, the flowfield of a helicopter rotor is generally more complex to analyze because it provides some of the most complex challenges to be found in the field of applied aerodynamics. This complexity stems from several peculiar problems that are unique to the helicopter rotor. These include a radially increasing blade speed that is responsible for a high concentration of bound circulation over the outer portion of the blade, resulting in a strong trailed tip vortex and a spiraling wake vortex sheet. The vortical wake initially remains close to the rotor, causing strong blade-vortex interactions. Other factors are the high centrifugal force field in which the blades operate, the relatively large steady-state out-of-plane displacement of the rotor blades and aeroelastic response of the rotor itself and, finally, mutual interaction of flowfields of main rotor, tail rotor, and the fuselage. These flowfields are often characterized by transonic conditions and associated shock waves, which make the flow more susceptible to three-dimensionality and unsteadiness.

The operating characteristics of such rotory-wing vehicles are strongly influenced by the vortex wake. The interaction of this wake with the following blades is a potential source of noise and vibration at low and moderate flight speeds. Accurate prediction of the vortical wake is probably the most important, most studied, and the most difficult aspect of helicopter flowfield. Current methods of analysis of the wake range in complexity from relatively simple momentum theory applications to free wake lifting surface methods.[1] The inadequacies of these methods have led to recent efforts to use state-of-the-art computational fluid dynamics (CFD) codes to shed more light on the understanding of this problem. Finite-difference codes for nonlinear compressible potential equations[2-6] and the Euler equations[7-14] have been used to calculate the rotor flowfields. Initially developed methods using the potential flow and the Euler formulations were primarily limited to calculating nonlifting rotor flow because of the inherent limitation of being unable to model the vortex wake with these equations, although the Euler formulation has in it the necessary physics to model vorticity transport correctly. These equations basically lack the physical mechanism needed to generate the vortex wake. However, in conjunction with

wake models contained in CAMRAD[15] and HOVER,[16] both potential flow and Euler codes have been used extensively to calculate the lifting rotor flowfields. The standard experimental data that is used in validating most of these codes has been the two-bladed rotor data of Carodonna and Tung.[17] An excellent review of some of the currently available inviscid finite-difference numerical methods have also been presented recently by Caradonna and Tung.[18]

As mentioned previously, tip vortices are an important part of the helicopter rotor flowfield. These vortices, which are generated at the tips of the rotating blades along with the helical wake vortex sheet, have tremendous influence on the operating characteristics of the rotor. Some of the common practical problems caused by such concentrated trailing vortices are the rotor vibration due to unsteady lift fluctuations, increased induced drag, and the annoying "blade-slap" (an impulsive noise characteristic). Many studies have been made to date to understand and reduce the influence of tip vortices by means of modifications to the tip geometry of the rotating blades. Most of the previous analytical and numerical studies are basically inviscid in nature and, therefore, preclude the physical mechanisms necessary to model correctly the formation of the tip vortex, which involves the complex three-dimensional viscous flowfield in the tip region.

The thin-layer Navier-Stokes simulations of tip flows have been attempted only recently after more powerful supercomputers became available. The studies of Mansour[19] and Srinivasan et al.,[20] show limited success in simulating the complex tip flows. Simulation of the complex vortex wake now appears possible with a proper Navier-Stokes algorithm, in conjunction with patched and/or zonal grid topology to discretize the flowfield. Understanding the mechanisms of the tip vortex formation and its subsequent rollup would provide a proper insight to control these tip flows and alleviate some of the problems caused by them. The ability to preserve the concentrated vortices in the finite-difference grid without numerical diffusion has been the biggest setback until now for progress in this area (see, for example, Ref. 21). Even the most advanced computational techniques, which use spatial central differencing, lack the proper mechanism to preserve concentrated tip vortices and convect them in the flowfield without numerical diffusion. However, the recently developed upwind schemes in conjunction with a proper grid choice appear very promising to preserve and convect concentrated vortices.[22] Alternatively, if the properly captured tip vortex is analytically represented, then prescribed vortex methods[23,24] could be applied to calculate the vortex wake development for several rotations of the blade. These methods have demonstrated the ability to preserve and convect concentrated vortices even in very coarse grid regions without significant numerical diffusion.

The use of Navier-Stokes codes to model the rotor flowfields have been limited in the past, primarily because of the large computer memory and CPU time requirements. In fact, these codes may not be more expensive to run than some of the Euler codes, but to have a meaningful flow definition in the tip region and in the wake might make such a procedure very expensive. Recently, Wake and Sankar[25] have presented some nonlifting and lifting calculations for a rotor in hover using a coarse grid with a poor definition of the tip region. The results for surface pressure are in fair agreement with experimental data. The lifting calculations used a correction to the geometric angle of attack of the blade obtained from the lifting surface code of Ref. 16. In the present study, using a fine grid in the tip region, thin-layer Navier-Stokes equations are solved for the flowfield of rectangular blade in hover with a view to also capture the tip vortex. Both nonlifting and lifting cases have been calculated with subcritical and supercritical tip Mach numbers. Surface pressure distributions and tip flow data are presented and compared with experimental data. Alternate methods of calculating the hover flowfield in a nonrotating mode (an isolated fixed blade), keeping the circulation distribution the same as that of a hovering blade, are explored, and the results for these are compared with the hover results.

Governing Equations and Numerical Scheme

The governing partial differential equations are the unsteady, thin-layer Navier-Stokes equations. For generality, these equations are transformed from the Cartesian reference frame (x,y,z,t) to the arbitrary curvilinear space (ξ,η,ζ,τ), while retaining strong conservation law form to capture shock waves. The transformed equations are given by[26]

$$\partial_\tau \hat{Q} + \delta_\xi \hat{F} + \partial_\eta \hat{G} + \partial_\zeta \hat{H} = Re^{-1} \partial_\zeta \hat{S} \tag{1}$$

where

$$\hat{Q} = J^{-1} \begin{bmatrix} \rho \\ \rho u \\ \rho v \\ \rho w \\ e \end{bmatrix}, \quad \hat{F} = J^{-1} \begin{bmatrix} \rho U \\ \rho u U + \xi_x p \\ \rho v U + \xi_y p \\ \rho w U + \xi_z p \\ U(e+p) - \xi_t p \end{bmatrix}$$

$$\hat{G} = J^{-1} \begin{bmatrix} \rho V \\ \rho u V + \eta_x p \\ \rho v V + \eta_y p \\ \rho w V + \eta_z p \\ V(e+p) - \eta_t p \end{bmatrix}, \quad \hat{H} = J^{-1} \begin{bmatrix} \rho W \\ \rho u W + \zeta_x p \\ \rho v W + \zeta_y p \\ \rho w W + \zeta_z p \\ W(e+p) - \zeta_t p \end{bmatrix} \tag{2}$$

The viscous flux vector $\hat{S}$, written here in the limit of thin-layer approximation, is given

$$\hat{S} = J^{-1} \begin{bmatrix} 0 \\ K_1 u_\zeta + K_2 \zeta_x \\ K_1 v_\zeta + K_2 \zeta_y \\ K_1 w_\zeta + K_2 \zeta_z \\ K_1 \{ Pr^{-1} (\gamma - 1)^{-1} (a^2)_\zeta + [(q^2)/2]_\zeta \} \\ + K_2 K_3 \end{bmatrix} \tag{3}$$

where

$$K_1 = \mu(\zeta_x^2 + \zeta_y^2 + \zeta_z^2) \tag{4a}$$

$$K_2 = \mu(\zeta_x u_\zeta + \zeta_y v_\zeta + \zeta_z w_\zeta)/3 \tag{4b}$$

$$K_3 = \zeta_x u + \zeta_y v + \zeta_z w \tag{4c}$$

$$q^2 = u^2 + v^2 + w^2 \tag{4d}$$

The primitive variables of Eq. (1), viz., the density ρ, the mass fluxes ρu, ρv, ρw, and the enregy per unit volume e, are normalized by the freestream reference quantities. The reference length scale is C, and the reference time scale is C/a_∞. The relations for the contravariant velocities U, V, and W, the Jacobian of transformation J, and the metrics of the transformation $(\xi_t,\xi_x,\xi_y,\xi_z)$, $(\eta_t,\eta_x,\eta_y,\eta_z)$ and $(\xi_t,\eta_x,\eta_y,\eta_z)$ and $(\zeta_t,\zeta_x,\zeta_y,y_z)$ can be found in Ref. 26.

The velocity components u, v, w and the pressure p are related to the total energy per unit volume e through the equa-

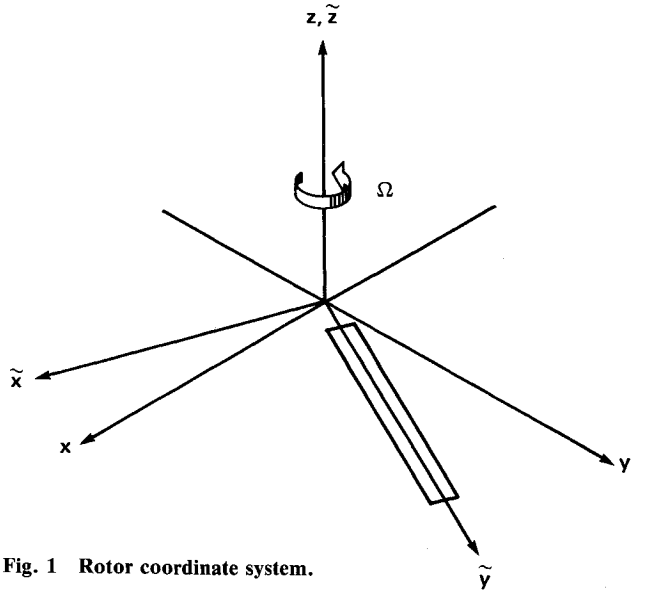

Fig. 1 Rotor coordinate system.

tion of state for a perfect gas by

$$p=(\gamma-1)\left[e-\frac{\rho}{2}(u^2+v^2+w^2)\right] \tag{5}$$

In the above equations, u, v, and w are the Cartesian components of the velocity in the inertial coordinate system (x,y,z,t). In the present formulation, Eq. (1) is solved in the inertial frame of reference. Figure 1 shows the inertial and blade-fixed coordinate system. The inertial coordinates $X=(x,y,z,t)$ are related to the blade-fixed coordinates $X_b=(\tilde{x},\tilde{y},\tilde{z},\tilde{t})$ through the relation given by

$$X(x,y,z)=\boldsymbol{R}(t)X_b(\tilde{x},\tilde{y},\tilde{z}) \tag{6a}$$

$$t=\tilde{t} \tag{6b}$$

where $\boldsymbol{R}(t)$ is the rotational matrix[27] given by

$$\boldsymbol{R}(t)=\begin{bmatrix}\cos\Omega\tilde{t} & -\sin\Omega\tilde{t} & 0\\ \sin\Omega\tilde{t} & \cos\Omega\tilde{t} & 0\\ 0 & 0 & 1\end{bmatrix} \tag{7}$$

Here, Ω is the rotational frequency of the rotor, and Ωt represents the azimuth sweep of the rotor blade. In view of Eq. (7), the metrics in inertial reference frame are related to those in the blade-fixed frame of reference through

$$\xi^i_x=\xi^i_{\tilde{x}}\cos\Omega\tilde{t}-\xi^i_{\tilde{y}}\sin\Omega\tilde{t} \tag{8a}$$

$$\xi^i_y=\xi^i_{\tilde{x}}\sin\Omega\tilde{t}+\xi^i_{\tilde{y}}\cos\Omega\tilde{t} \tag{8b}$$

$$\xi^i_z=\xi^i_{\tilde{z}} \tag{8c}$$

$$\xi^i_t=\Omega\tilde{y}\xi^i_{\tilde{x}}-\Omega\tilde{x}\xi^i_{\tilde{y}} \tag{8d}$$

where $\xi^i=\xi$, η, and ζ for $i=1$, 2, and 3, respectively.

The equation set (1) is solved using an implicit, approximately factored numerical scheme that uses spatial central differencing in the η and ζ directions, and upwind differencing in the ξ direction developed by Ying et al.[28] The flux vector $\hat{F}$ hasbeen split into $\hat{F}^+$ and $\hat{F}^-$ according to its eigenvalues. The factored operators are solved by sweeping in the ξ direction and inverting tridiagonal matrices with 5×5 blocks for the other two directions. Currently, a significant part of the computational time is taken to form the plus and minus Jacobian matrices for the flux vector $\hat{F}$ with this numerical scheme. Artificial dissipation terms(second- and fourth-order) have been added in the central-differencing directions for stability reasons.[26] The numerical code is vectorized for the Cray-2 supercomputer.

A body-conforming finite-difference grid has been used for the rectangular blade having a rounded-tip cap and consists of warped spherical O-O grid topology. The flowfield grid is numerically generated using the three-dimensional hyperbolic grid solver of Steger and Chaussee[29] with proper clustering in the leading- and trailing-edge regions and in the tip region. The grid is nearly orthogonal at the surface, and the spacing in the normal direction at the surface is chosen to be $0.00006C$. All of the computations were done with one grid topology having 155 points in the periodic direction around the airfoil, and 66 points each in the spanwise and normal directions, for a total of about 700,000 grid points. The outer grid boundary is chosen to be at 10 chords in all directions.

The boundary conditions consist of surface boundary conditions and far-field boundary conditions and are applied explicitly. For the nonrotating blade, the no-slip condition is enforced at the wall by setting U, V, and W to be zero, and ξ_t, η_t, and ζ_t are zero as the grid is stationary. For the rotating blade, however, U, V, and W are still set to zero, but ξ_t, η_t, and ζ_t are nonzero as the blade (and the grid attached to it) is moving in azimuth. Also, the density at the wall is determined by assuming an adiabatic wall condition. The pressure along the body surface is calculated from the normal momentum relation (see, for example, Ref. 26). Having calculated the density and pressure, the total energy is determined from the equation of state.

At the far-field boundary, the flow quantities are either fixed or extrapolated from the interior, depending on whether the flow is subsonic or supersonic and if it is of inflow or outflow type at the boundary. The characteristic velocities of the Euler equations determine the number of flow properties to be specified to control the reflections of waves from the boundaries. For the subsonic inflow boundary, four quantities must be specified. Thus, density is extrapolated, whereas the velocities and the total energy are specified by the freestream values. For the supersonic inflow, all flow quantities are specified. At the subsonic outflow boundaries, only one quantity is specified, viz., pressure is fixed and the other quantities are extrapolated. For the supersonic outflow condition, all flow quantities are extrapolated from the interior. At the plane containing the blade root, the condition $\partial Q/\partial y=0$ is imposed.

Results and Discussion

Both time-accurate and time-asymptotic (steady-state) calculations are performed in this study for an aspect ratio 6 rectangular blade having no twist or taper. The blade, which is a representative of a model two-bladed test rotor of Caradonna and Tung,[17] has a round tip cap (body of revolution) and is made up of NACA 0012 airfoil sections. The rotating blade calculations have been chosen to correspond to the model-hovering rotor experimental test conditions of Caradonna and Tung.[17] At the Reynolds number corresponding to the tip speeds in this test, the boundary layer can be assumed to be turbulent over the entire blade, and the Baldwin and Lomax algebraic turbulence model[30] is used to calculate the turbulent eddy viscosity. A typical solution, with vectorized code for the Cray-2, required about 700–1000 marching steps (approximately 45–60 deg of azimuth travel) to reach quasisteady flow conditions with CPU time per time step per grid point of 8.5×10^{-5} s. Time-accurate calculations were run with a maximum value for the time step of $\Delta t=0.01$, whereas the fixed-blade option used a variable time-step option[21] with $\Delta t=5$ to calculate steady-state flowfield. The maximum CFL numbers corresponding to the time-step size for the two cases are approximately 200 and 50, respectively.

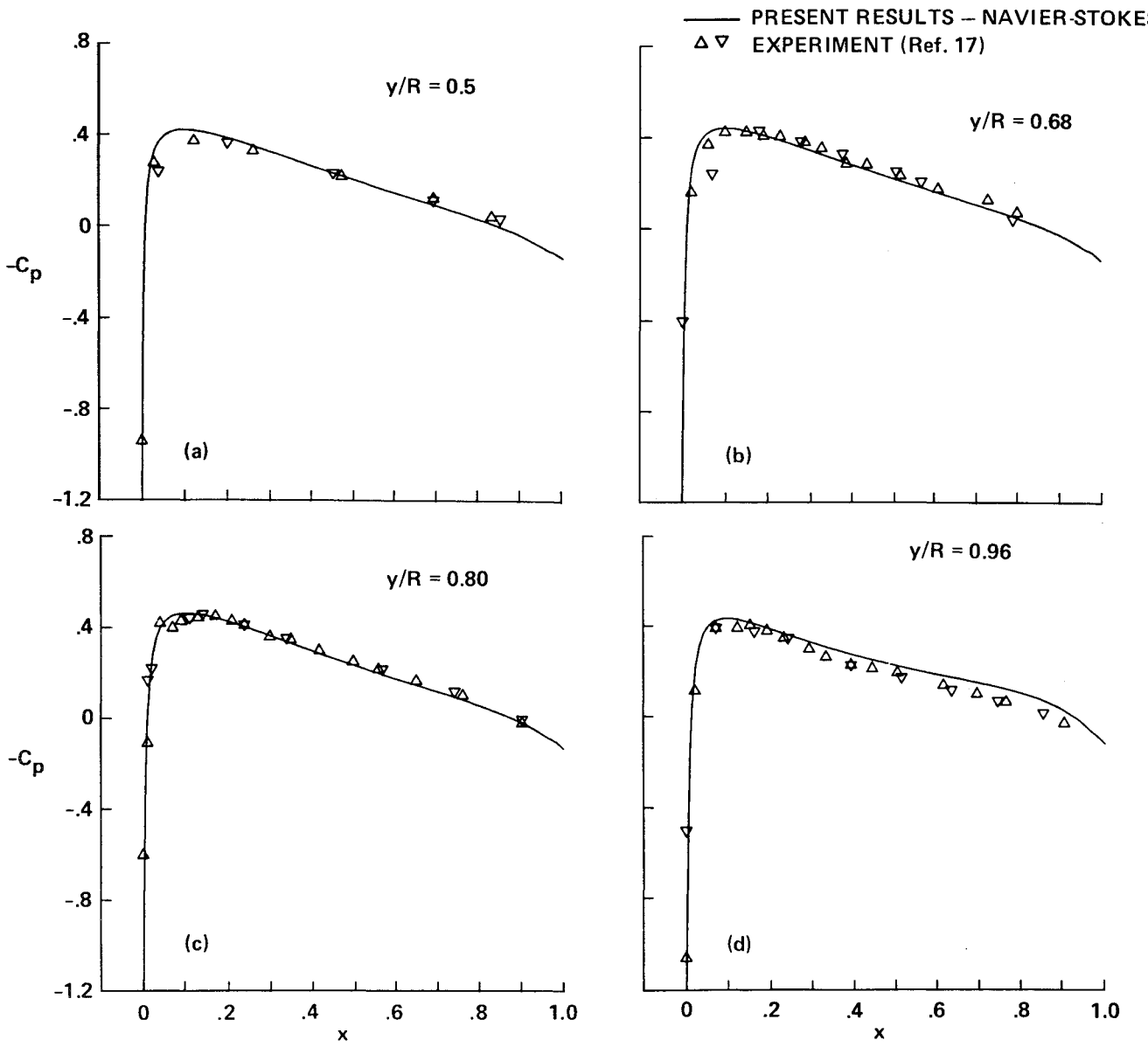

Fig. 2 Surface pressure distributions on a nonlifting rotor in hover, $M_{tip} = 0.52$, $Re = 2.32 \times 10^6$.

Hovering Blade

In the present approach, hover calculations are performed in a time-accurate fashion, since it is easily extendable to the forward-flight case. In reality, a hovering rotor flowfield is quasisteady in a blade-fixed coordinate system; but since the governing equations are solved in the inertial reference frame in the present approach, the flowfield never reaches steady state in this reference frame.

Figure 2 shows the chordwise surface pressure distributions at several radial stations for the nonlifting rotor with a tip Mach number $M_{tip} = 0.52$. The corresponding Reynolds number for this case is 2.32 million. The calculated results are in excellent agreement with experimental data at all radial stations.

Accurate calculation of lifting rotor flowfield is possible only if the induced effects of the wake are properly included in the analysis. In a recent review of current inviscid finite-difference rotor flow codes, Caradonna and Tung[18] have compared the numerical results from these codes that combine the finite-difference computations with several existing integral aerodynamics, loads, and trim codes. The simplest implementation is a spanwise twist correction to the blade to account for wake-induced effects. Recently, such an approach has been adopted by Agarwal and Deese[11] in a finite-volume Euler code to calculate the flowfield of hovering rotor corresponding to the wind-tunnel model test conditions of Caradonna and Tung.[17] They found that the induced downwash angle (given by the ratio of sectional induced velocity to the local blade speed), calculated from a free-wake analysis program corresponding to the experimental conditions, is nearly constant ($= -3.8$ deg) over a large part of the blade span ($0.4R - 0.9R$) and for the entire range of test conditions for this particular rotor. With this observation, they assumed a constant induced flow angle at the blade surface due to the wake and corrected the blade pitch angle. Their numerical results agreed well with the experimental data except that the shock wave position was predicted downstream of the experiments at the supercritical flow condition. To facilitate comparisons with the inviscid results of Agarwal and Deese,[11] the present viscous study also assumes a constant induced angle of -3.8 deg for the entire blade.

Using this simplified wake model for the Caradonna and Tung[17] rotor with a collective pitch of 8 deg, lifting calculations were performed for hovering blades set at an effective pitch of 4.2 deg and having tip Mach numbers of 0.44 and 0.877 (with corresponding thrust coefficients of $C_T = 0.0046$

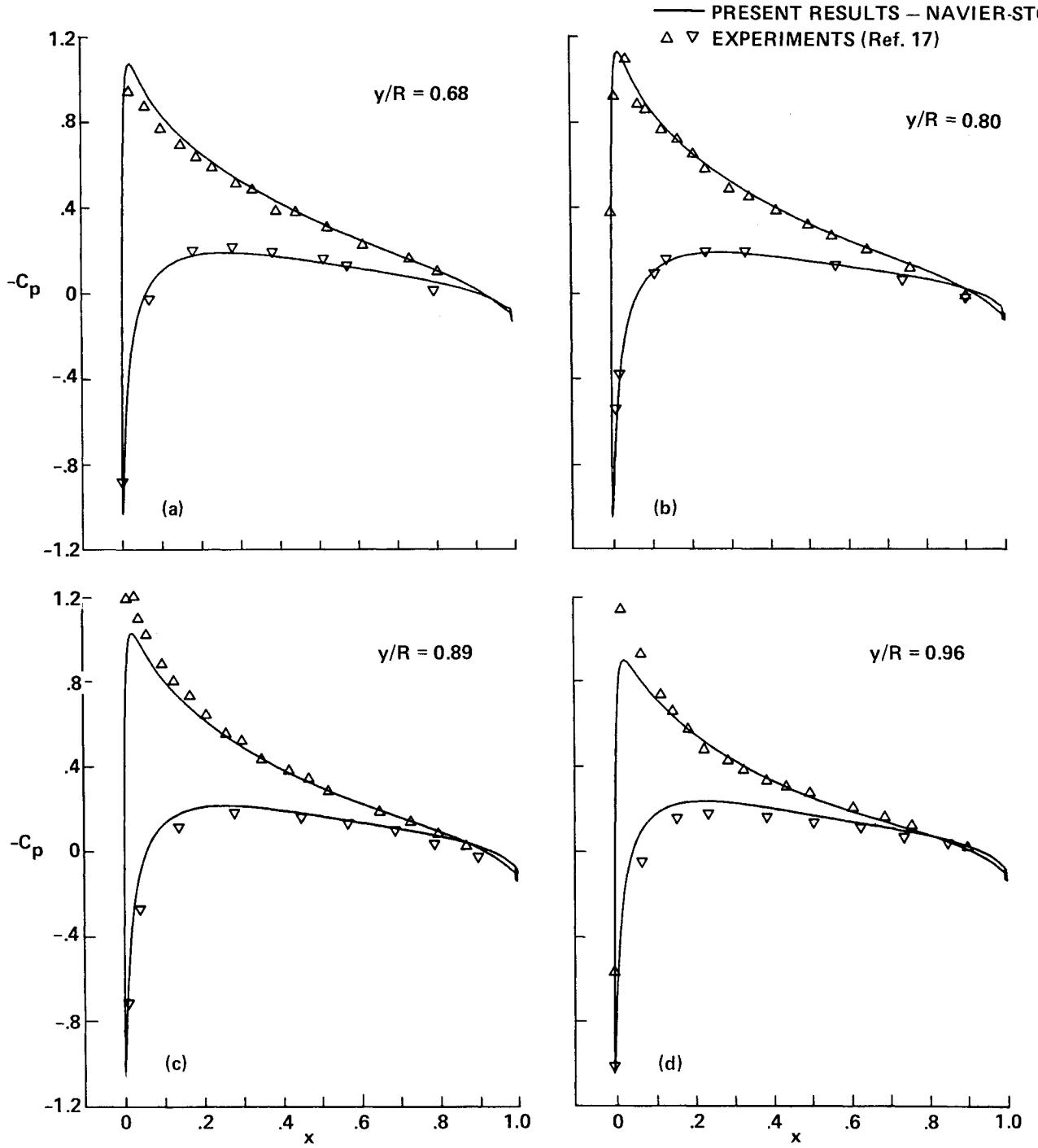

Fig. 3 Surface pressure distributions on a lifting rotor in hover, $M_{tip} = 0.44$, $\theta_{eff} = 4.2$ deg, $Re = 1.9 \times 10^6$.

and 0.00464), respectively. Figures 3 and 4 show the computed results for these cases in the form of surface pressure distributions for representative blade radial stations compared with the experimental data. The comparison shows very good agreement for the radial stations between 0.5 to 0.95 of radius, for both subcritical and supercritical cases. The agreement progressively deteriorates for radial stations less than $0.5R$, which is probably due to the crude wake model used here. As previously noted, Agarwal and Deese[11] have also calculated the same flow using the finite-volume Euler formulation and the same induced downwash correction. They also get a similar agreement with the experimental data for the subcritical case. However, their predictions of shock locations are downstream of the measurements for the supercritical case, thus indicating that viscous effects are important in this case.

Additional flowfield data are presented in Figs. 5–7 for the supercritical lifting case configuration corresponding to a tip Mach number of $M_{tip} = 0.877$. It is well known that the formation of the tip vortex involves complex three-dimensional flow separation in the tip region. Figure 5a shows a view of the surface particle flow traces in the tip region of this rotating blade. This view is generated by releasing fluid particle tracers at one grid point above the surface and confining the flow to stay in that plane. This view is supposed to mimic the surface oil flow pattern often used in wind-tunnel experiments. The separation and reattachment lines of the flow are marked by the letters S and R, respectively, in Fig. 5a. The extent of separation on the upper surface, inboard of the tip, is much larger compared to the mild separation seen on the lower surface in the tip region. A similar observation is also made for the subcritical lifting

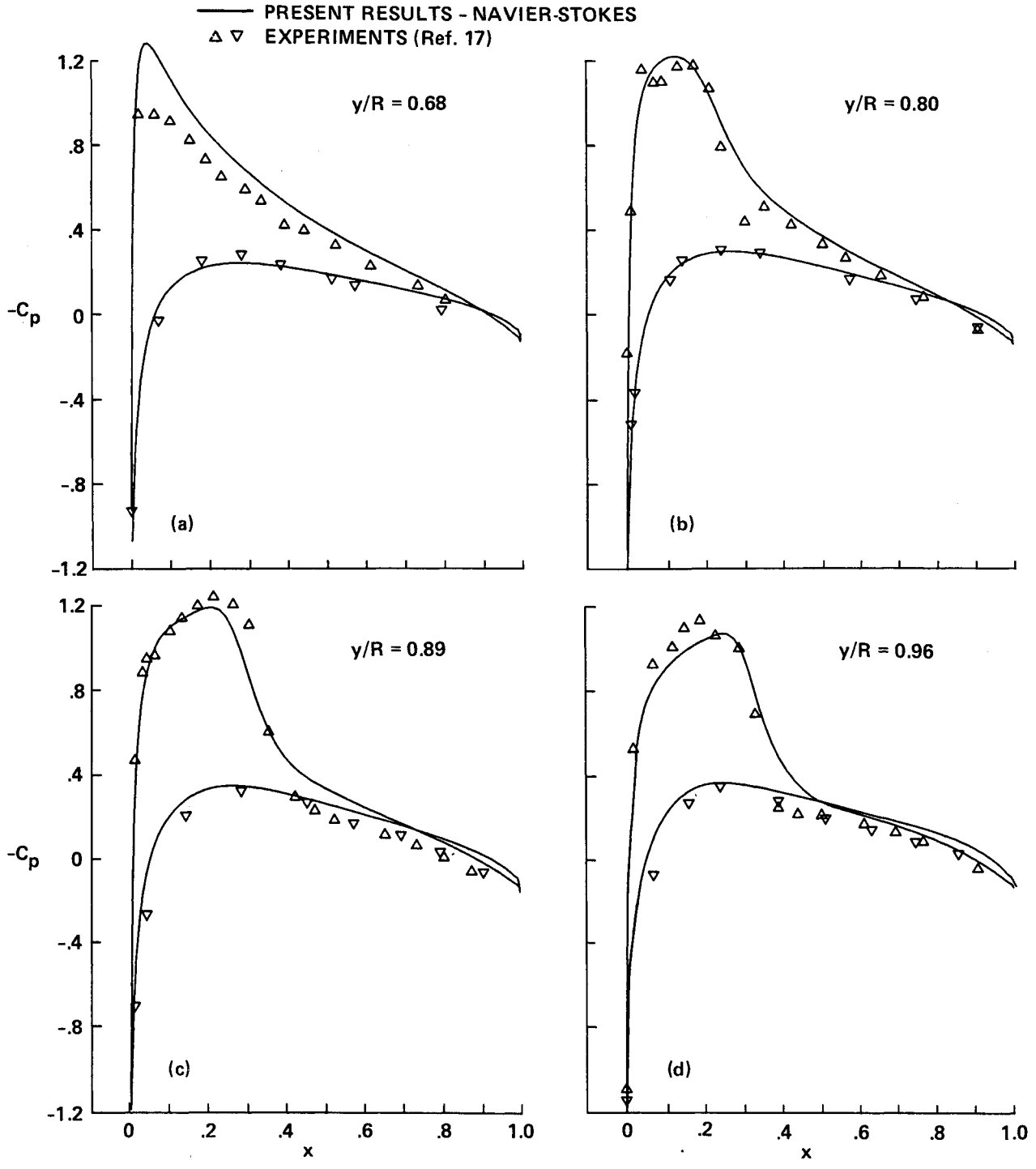

Fig. 4 Surface pressure distributions on a lifting rotor in hover, $M_{tip} = 0.877$, $\theta_{eff} = 4.2$ deg, $Re = 3.93 \times 10^6$.

case corresponding to $M_{tip} = 0.44$, and the results are presented elsewhere.[31] For the supercritical case, however, there is a strong shock wave on the upper surface of the blade in the tip region, as shown by the pressure contour plot of Fig. 6a. This may also be affecting the extent of separated region. As seen in this figure, the shock wave becomes very weak and almost vanishes in the vicinity of the blade tip due to the tip relief action.

The braiding together of unrestricted fluid particle tracers released from different locations on the upper and lower surfaces of the blade in the tip region shows the formation process of the tip vortex (Fig. 7a). In contrast to a nonrotating blade,[20] the process of braiding of fluid particle tracers from upper and lower surfaces is delayed until after the vortex lifts off from the upper surface. As seen in the view looking at the tip in Fig. 7a, the initial braiding process is comprised mostly of the particles released from the upper surface, and the vortex lifts off from the separated region inboard of the tip. The braiding process continues in the wake region during the rollup process with particles from both upper and lower surfaces. The strength of this vortex is determined, as in Ref. 20, by taking a line integral of the velocity vector over a closed path enclosing the vortex. Estimations done at several locations in the downstream wake by this method gave a value of 0.07 to 0.08 for the (nondimensional) tip vortex strength depending on the path of the line integral. In comparison, the integrated lift coefficient C_L from the blade surface pressure distributions was found to be 0.17, implying $\Gamma_V = 0.085$. A

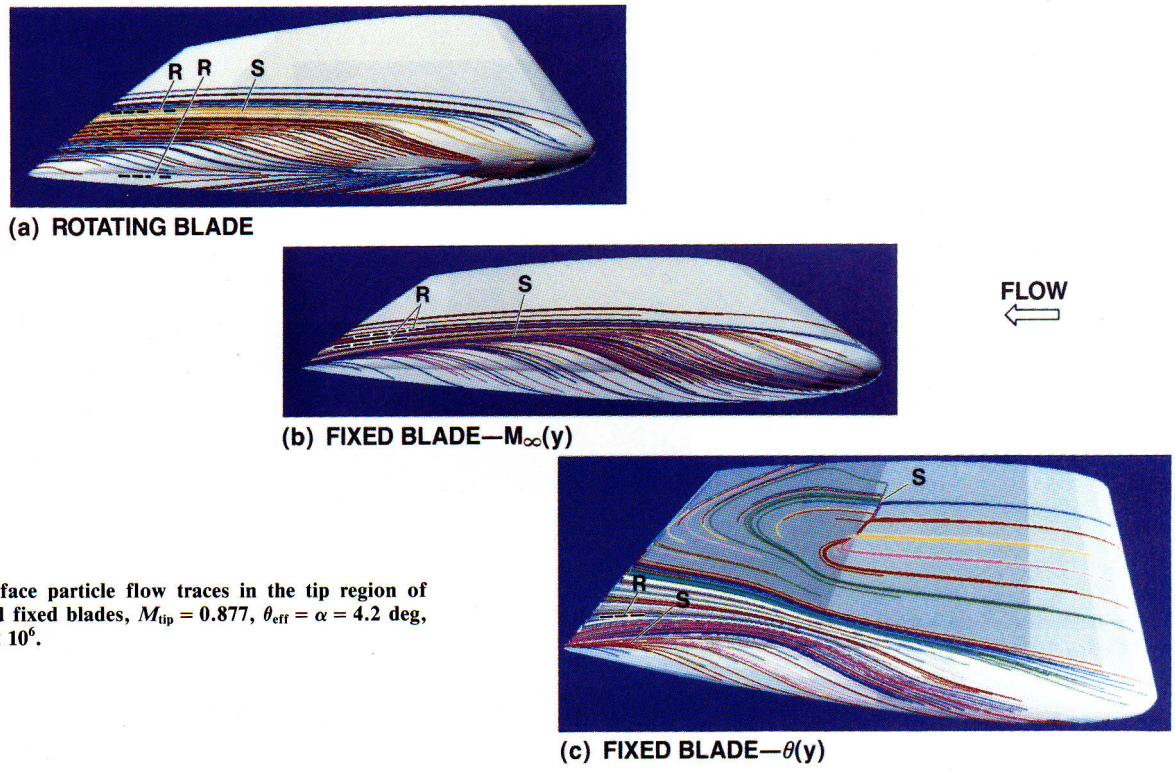

Fig. 5 Surface particle flow traces in the tip region of rotating and fixed blades, $M_{tip} = 0.877$, $\theta_{eff} = \alpha = 4.2$ deg, $Re = 3.93 \times 10^6$.

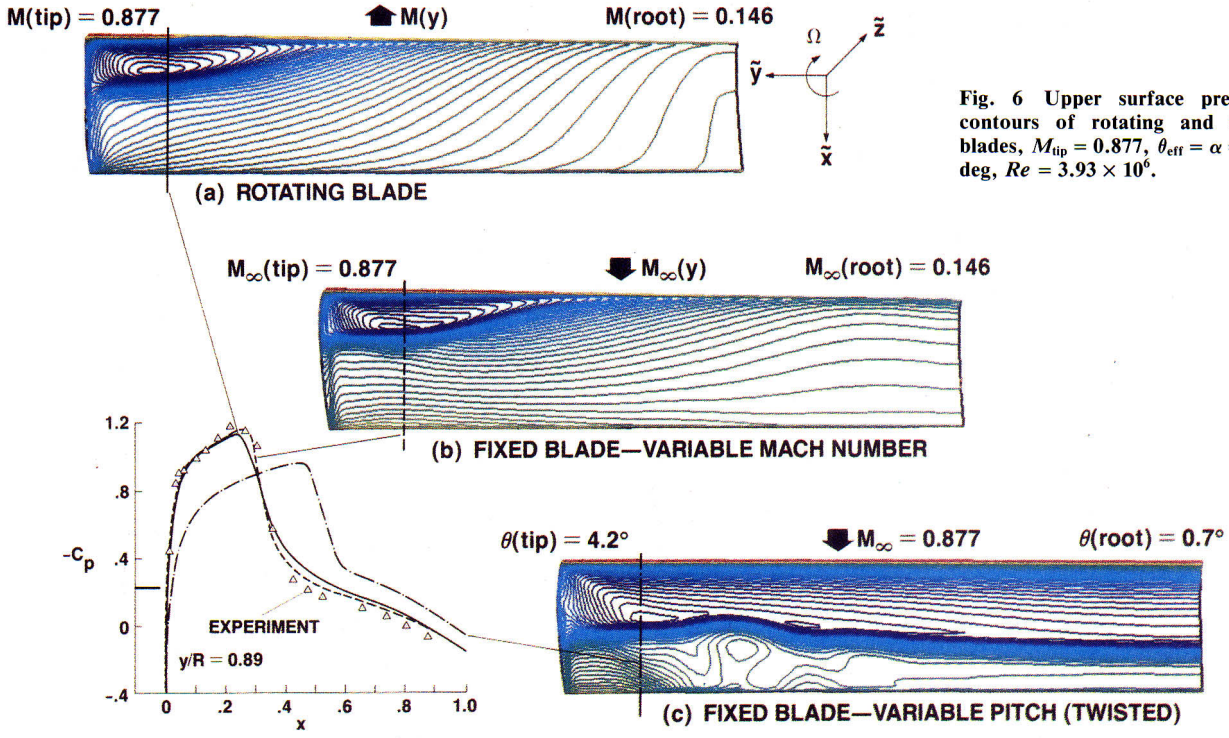

Fig. 6 Upper surface pressure contours of rotating and fixed blades, $M_{tip} = 0.877$, $\theta_{eff} = \alpha = 4.2$ deg, $Re = 3.93 \times 10^6$.

similar estimate made for the subcritical case gave a nondimensional tip vortex stength of about 0.08. From this, it appears that the nondimensional tip vortex strength is relatively independent of the blade tip Mach number as observed in the experiments.[17] For qualitative viewing of tip vortex shape, size and strength, Fig. 7a also shows inserts of vorticity contour plots at two locations in the wake region. These contour plots are drawn in the y-z plane and demonstrate how the vortex that has a tight structure initially ($\tilde{x} = 1.0$) gets diffused in downstream coarse grid regions ($\tilde{x} = 4.6$).

Fixed Blade

The results presented in the previous section for the hovering blade were computed in a time-accurate manner. These are, therefore, time-consuming and expensive. This section explores alternate methods to compute the quasisteady flowfield of the hovering rotor, in particular, like the flowfield of a fixed blade with approximately the same circulation distribution as that of the hovering rotor blade with the same tip Mach number. One can achieve this for a given blade planform in three different ways. These are 1) having the flow Mach

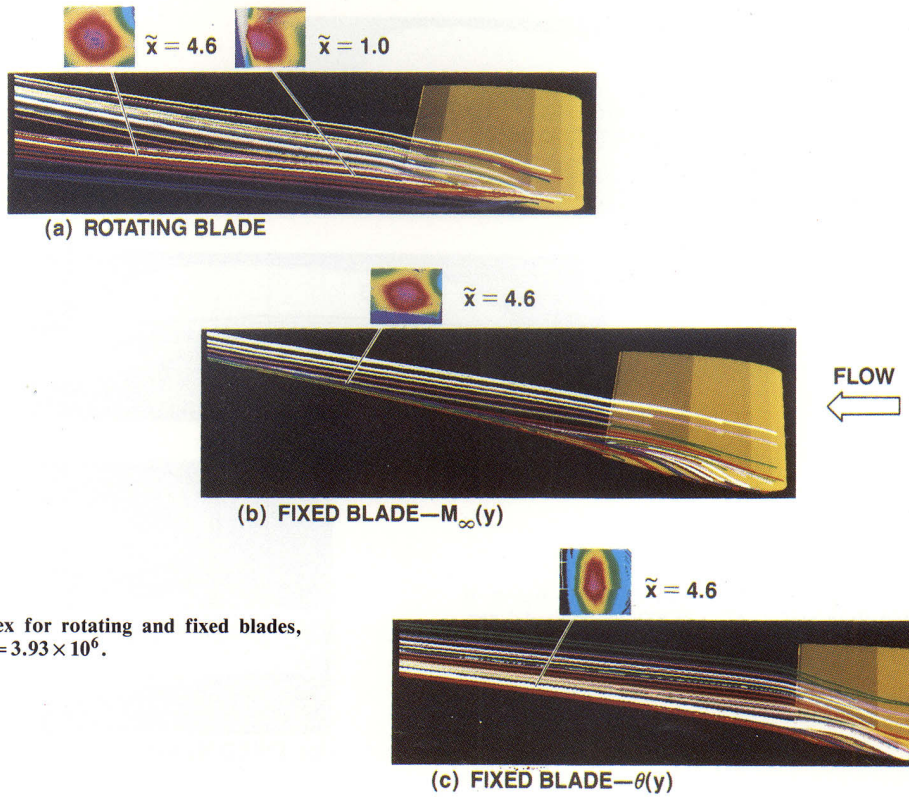

Fig. 7 Far-field view of tip vortex for rotating and fixed blades, $M_{tip} = 0.877$, $\theta_{eff} = \alpha = 4.2$ deg, $Re = 3.93 \times 10^6$.

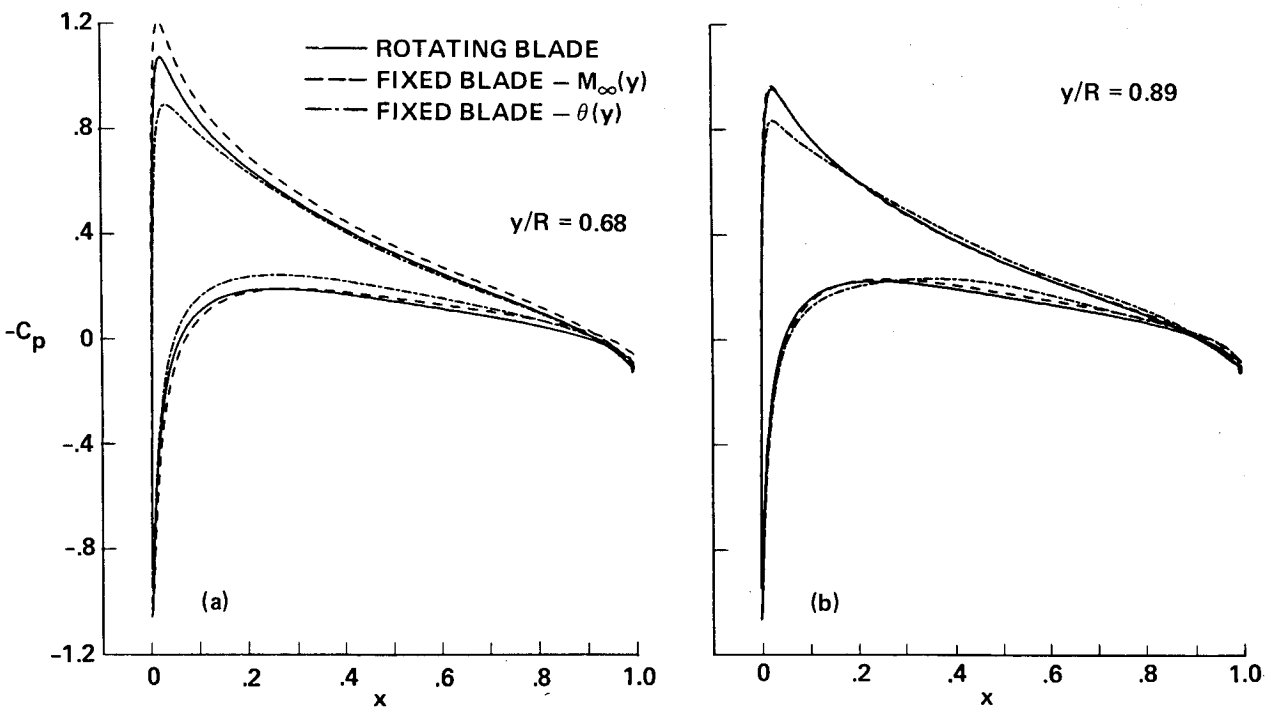

Fig. 8 Surface pressure distributions for fixed and rotating blades in subcritical flow, $M_{tip} = 0.44$, $\theta_{eff} = \alpha = 4.2$ deg, $Re = 1.92 \times 10^6$.

number distributed as a function of the radial distance exactly like a hovering blade, keeping everything else the same, 2) keeping the flow Mach number uniform for the entire blade equal to the tip speed and then having a twist distribution along the blade, which decreases from the tip to the root of the blade, and 3) keeping the flow uniform as in No. 2, but increase the chord of the blade uniformly from the root to the tip. In the following, only the results for the first two options are presented.

Navier-Stokes steady-state flowfields were calculated for these nonrotating configurations using a variable time-step option[21] to accelerate the convergence rate of the numerical procedure. The results are presented in Figs. 5–9. Figures 8 and 9 show typical results in the form of surface pressure distributions, compared with the hovering rotor results for both subcritical and supercritical cases. The subcritical results presented in Fig. 8 show a surprisingly good agreement with the hover results for both the options of variable twist and

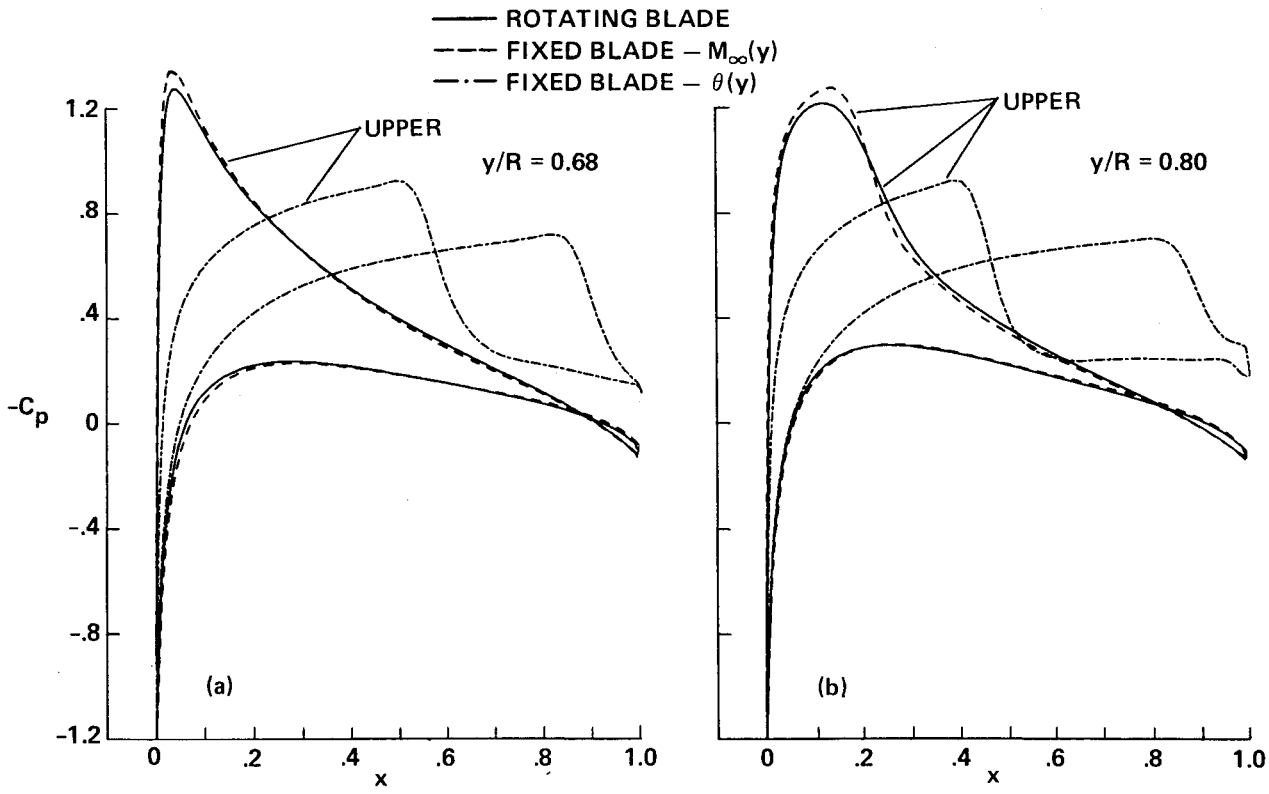

Fig. 9 Surface pressure distributions for fixed and rotating blades in subcritical flow, $M_{tip} = 0.877$, $\theta_{eff} = \alpha = 4.2$ deg, $Re = 3.93 \times 10^6$.

variable Mach number. Considering the close agreement of the results even at the radial station near the tip of the blade, the influence of the centrifugal forces present in the rotating blade seem to have very little influence in modifying the pressure field in the tip region. There are very small differences in the surface particle flow patterns and the locations of vortex liftoff from the surface for these cases compared to the hovering blade.[31] The fixed-blade configurations seem to produce a tightly braided vortex structure even before leaving the blade surface, but its strength appears to be within 5-10% of the corresponding hovering blade value.

The supercritical results presented in Figs. 5 and 9 for the two options of fixed-blade mode show that the flow is dominated by the transonic shocks. Even then the results for the variable Mach number case show remarkably good agreements with the results of the hovering case, as seen in Figs. 6a and 6b. However, the variable twist option, shown in Fig. 6c, gives results that are totally different from the hovering results at this transonic condition, as seen from the surface pressure distributions of Fig. 9. This is not surprising for the *inboard* part of the blade, since a high flow Mach number (equal to tip Mach number of rotor) exists all along the span for this nonrotating case. However, even the *tip* region is significantly different in this case. Comparison of upper surface pressure distributions in the form of contour plots for these cases, shown in Figs. 6b and 6c, with that of hovering blade result of Fig. 6a, demonstrates the closeness of the variable Mach number, fixed-blade option to the hovering case. The variable twist, fixed Mach-number (uniform flow) case produces too strong a shock wave along the entire blade with the consequence of producing a totally different flowfield. In fact, the severity of the constant uniform freestream Mach number along the entire span is also evident from the presence of a strong shock wave, even on the lower surface for this case, as seen in Fig. 9.

The close agreement of the surface pressure distributions for the cases of Figs. 6a and 6b suggests that even at this supercritical flow condition, the influence of the centrifugal forces has a minimal effect on the overall flowfield. However, the surface particle flow patterns, seen in Figs. 5a–c, show differences in the flowfields in the tip region for these cases. Although the rotating-blade case of Fig. 5a and the fixed-blade case of Fig. 5b have similar surface pressure distributions, the surface flow in the tip region appears different. The primary difference between the two cases appears to occur in the viscous layers, i.e., the presence of centrifugal force in the rotating-blade case has produced a small-scale local separation on the lower surface of the tip in addition to the separation seen on the upper surface of the blade. This mild separation is clearly seen in Fig. 5a. The surface oil patterns on the tip caps for the fixed-blade cases of Figs. 5b and 5c appear similar, even though the flowfield for the case of Fig. 5c is dominated by the strong transonic shock wave and its associated effects.

The views of the tip vortices shown in Fig. 7 for these cases appear nearly identical, although the liftoff of the tip vortex for hovering blade occurs well inboard of the tip on the upper surface, in contrast to the fixed blade cases of Figs. 7b and 7c, for which the liftoff appears to occur right at the tip on the upper surface of the blade. The far-field views of the tip vortices presented in Fig. 7 show the initial formation process the liftoff, and rollup in the wake. Also shown here are the vorticity contour plots (insert). These vorticity contour plots are made by slicing the tip vortices in the y-z plane to demonstrate the relative shape, size, and strength as well. Estimates made for the tip vortex strengths have revealed that the variable Mach number case is almost identical to that of the hovering blade case. The variable twist case, on the other hand, produced a much higher lift and a vortex strength approximately 2.5 times that of the hovering case. The vortex shapes and sizes are qualitatively determined by the vorticity contour plots shown in Fig. 7. Although the shape and size for the cases of Figs. 7a and 7b appear to be nearly identical, the case of Fig. 7c appears to be very tightly braided, but stretched slightly in vertical direction. All of the calculations presented here have been done on the same grid topology to remove any grid dependency from the comparisons.

Conclusions

Unsteady, thin-layer Navier-Stokes equations written in rotor coordinates are solved using a flux-split approximately factored, implicit, numerical algorithm to calculate the quasi-steady flowfield of a hovering rotor blade. The test cases chosen correspond to the experimental model hover test conditions of Caradonna and Tung.[17] The induced wake effects in the lifting calculations were accounted as a correction to the geometric angle of attack. The numerical results compare very well with the experimental data for both nonlifting and lifting cases. Alternate methods were explored to calculate the hovering rotor flowfield as a steady-state flowfield on a fixed isolated blade, keeping the same circulation distribution as that of the hovering blade. Of the two options considered, the variable freestream Mach number case gave almost identical pressure distributions as that of rotor at both subcritical and supercritical flow conditions. The variable twist option, on the other hand, gave similar results only under subcritical flow conditions; the supercritical flow condition was dominated by stronger transonic shocks even in the tip region. Under conditions where the fixed blade flowfield closely agreed with that of the hovering blade, the influence of the centrifugal forces of the rotating blade appeared to have minimum influence on the overall flowfield properties. Although these conclusions are preliminary and primarily based on the comparison of surface pressures and vortex strength estimates, further quantitative comparison of the vortex structure is needed for a clear understanding of the similarities and differences.

Acknowledgments

The first author would like to acknowledge the support of this research by the U.S. Army Research Office under Contract DAAG29-85-C-0002 with Drs. R.E. Singleton and T.L. Doligalski as Technical Monitors. Computational support is provided by Dr. T.L. Holst, Chief of Applied Computational Fluids Branch at NASA Ames Research Center. The authors would like to thank Dr. J.L. Steger for many helpful discussions. The graphics work presented here was generated using PLOT3D package developed by Dr. P.G. Buning at NASA Ames Research Center.

References

[1]Landgrebe, A.J., "Overview of Helicopter Wake and Airloads Technology," Twelfth European Rotorcraft Forum, Paper No. 18, Garmisch-Partenkirchen, Germany, Sept. 1986.

[2]Caradonna, F.X. and Isom, M.P., "Subsonic and Transonic Potential Flow over Helicopter Rotor Blades," *AIAA Journal,* Vol. 10, Dec. 1972, p. 1606-1612.

[3]Chang, I.-C., "Transonic Flow Analysis for Rotors," NASA TP-2375, 1984.

[4]Strawn, R.C. and Caradonna, F.X., "Conservative Full-Potential Model for Unsteady Transonic Rotor Flows," *AIAA Journal,* Vol. 25, Feb. 1987, pp. 193-1981

[5]Steinhoff, J. and Ramachandran, K., "Free Wake Analysis of Compressible Rotor Flows," AIAA Paper 87-0542, Jan. 1987.

[6]Sankar, L.N. and Prichard, D., "Solution of Transonic Flow Past Rotor Blades Using the Conservative Full Potential Equation," AIAA Paper 85-5012, Oct. 1985.

[7]Wake, B.E., Sankar, N.L., and Lekoudis, S.G., "Computation of Rotor Blade Flows Using the Euler Equations," *Journal of Aircraft,* Vol. 23, July 1986, pp. 582-588.

[8]Chen C.L. and McCroskey, W.J., "Numerical Simulation of Helicopter Multi-Blade Rotor Flow," AIAA Paper 88-0046, Jan. 1988.

[9]Roberts, T.W. and Murman, E.M., "Solution Method for a Hovering Helicopter Rotor using the Euler Equations," AIAA Paper 85-0436, Jan. 1985.

[10]Kroll, N., "Computations of the Flow Fields of Propellers and Hovering Rotor using Euler Equations," Twelfth European Rotorcraft Forum, Paper No. 28, Garmisch-Partenkirchen, Germany, Sept. 1986.

[11]Agarwal, R.K. and Deese, J.E., "Euler Calculations for Flowfield of a Helicopter Rotor in Hover," *Journal of Aircraft,* Vol. 24, April 1987, pp. 231-238.

[12]Sankar, N.L. and Tung, C., "Euler Calculations for Rotor Configurations in Unsteady Forward Flight," *Proceedings of the 42nd Annual Forum of American Helicopter Society,* Washington, DC, June 1986, pp. 985-995.

[13]Chang, I-C., and Tung, C., "Euler Solution of the Transonic Flow for a Helicopter Rotor," AIAA Paper 87-0523, Jan. 1987.

[14]Agarwal, R.K. and Deese, J.E., "An Euler Solver for Calculating the Flowfield of a Helicopter Rotor in Hover and Forward Flight," AIAA Paper 87-1427, June 1987.

[15]Johnson, W., "A Comprehensive Analytical Model of Rotorcraft Aerodynamics, Part 1, Analysis Development," NASA TM-81182, June 1980.

[16]Summa, J.M. and Clark, D.R., "A Lifting-Surface Method for Hover/Climb Airloads," *Proceedings of the 35th Annual Forum of the American Helicopter Society,* Washington, DC, May 1979.

[17]Caradonna, F.X. and Tung, C., "Experimental and Analytical Studies of a Model Helicopter Rotor in Hover," NASA TM-81232, Sept. 1981.

[18]Caradonna, F.X. and Tung, C., "A Review of Current Finite Difference Rotor Flow Codes," *Proceedings of the 42nd Annual Forum of the American Helicopter Society,* Washington, D.C., June 1986, pp.967-983.

[19]Mansour, N.N., "Numerical Simulation of the Tip Vortex Off a Low-Aspect Ratio Wing at Transonic Speed," *AIAA Journal,* Vol. 23, Aug. 1985, pp. 1143-1149.

[20]Srinivasan, G.R., McCroskey, W.J., Baeder, J.D., and Edwards, T.A., "Numerical Simulation of Tip Vortices of Wings in Subsonic and Transonic Flows," AIAA Paper 86-1095, May 1986.

[21]Srinivasan, G.R., Chyu, W.J., and Steger, J.L., "Computation of Simple Three-Dimensional Wing-Vortex Interaction in Transonic Flow," AIAA Paper 81-1206, June 1981.

[22]Rai, M.M., "Navier-Stokes Simulations of Blade-Vortex Interaction Using High-Order Accurate Upwind Schemes," AIAA Paper 87-0543, Jan. 1987.

[23]Steinhoff, J. and Suryanarayanan, K., "The Treatment of Vortex Sheets in Compressible Potential Flow," AIAA Paper 83-1881-CP, July 1983.

[24]Srinivasan, G.R. and McCroskey, W.J., "Numerical Simulations of Unsteady Airfoil-Vortex Intractions," *VERTICA,* Vol. 11 No. 1/2, 1987, pp. 3-28.

[25]Wake, B.E. and Sankar, L.N., "Solutions of the Navier-Stokes Equations for the Flow About a Rotor Blade," *Proceedings of National Specialists' Meeting on Aerodynamics and Aeroacoustics,* Arlington, TX, Feb. 1987.

[26]Pulliam, T.H. and Steger, J.L., "Implicit Finite-Difference Simulations of Three-Dimensional Compressible Flow," *AIAA Journal,* Vol. 18, Feb. 1980, pp. 159-167.

[27]Isom, M.P., "Unsteady Subsonic and Transonic Potential Flow over Helicopter Rotor Blades," NASA CR-2463, Oct. 1974.

[28]Ying, S.X., Steger, J.L., Schiff, L.B., and Baganoff, D., "Numerical Simulation of Unsteady, Viscous, High-Angle-Of-Attack Flows Using a Partially Flux-Split Algorithm," AIAA Paper 86-2179, Aug. 1986.

[29]Steger, J.L. and Chaussee, D.S., "Generation of Body-Fitted Coordinates Using Hyperbolic Partial Differential Equations," *SIAM Journal on Scientific and Statistical Computing,* Vol. 1, Dec. 1980, pp. 431-437.

[30]Baldwin, B.S. and Lomax, H., "Thin Layer Approximation and Algebraic Model for Separated Turbulent Flow," AIAA Paper 78-257, Jan. 1978.

[31]Srinivasan, G.R. and McCroskey, W.J., "Navier-Stokes Calculations of Hovering Rotor Flowfields," AIAA Paper 87-2629-CP, Aug. 1987.

Color reproduction courtesy of NASA Ames Research Center.